

# Nitric Oxide Delivery across the Stratum Corneum Mediated by Chitosan Nanogels: A Coarse-Grained Molecular Dynamics Study

Neila Cristina Fonseca Machado, Roberta Albino Dos Reis, Rena Silva Nunes, Nicolás Ariel Garcia, Amedea Barozzi Seabra, Herculano da Silva Martinho

## Abstract

Nitric oxide (NO) delivery across the stratum corneum (SC) remains a major challenge due to the highly ordered, architecture of this skin barrier and the short lifetime of NO. In this work, coarse-grained molecular dynamics simulations are employed to investigate how chitosan-based nanogels loaded with S-nitrosoglutathione (GSNO) mediate NO delivery at the SC interface. We used two approaches, with and without the use of a physical enhancer, in this case, a constant electric field. In the absence of an electric field, the chitosan-TPP-GSNO nanogel preserves a cohesive polymeric architecture and adsorbs stably at the membrane surface through protonated chitosan-headgroup interactions. This adsorption induces only mild leaflet compaction, while lamellar thickness and lipid mobility remain essentially unaltered, demonstrating that the nanogel acts as a compliant, surface-anchored reservoir that preserves barrier integrity. Within this architecture, GSNO remains confined in a partially hydrated peripheral region of the nanogel, providing localized interfacial availability of NO without uncontrolled diffusion into the membrane core. Using electric fields, simulations further reveal that external electric fields can actively modulate GSNO behavior by triggering non-equilibrium membrane remodeling events, including vesicle formation and conductive pore opening, which create transient pathways for GSNO transport across the SC. By resolving nanogel structure, interfacial contacts, membrane response, and GSNO trajectories at the molecular level, this study provides an integrated mechanistic picture of how nanogel-mediated confinement and membrane remodeling jointly regulate NO delivery across the stratum corneum.

Cite this: DOI: 00.0000/xxxxxxxxxx

# Nitric Oxide Delivery across the Stratum Corneum Mediated by Chitosan Nanogels: A Coarse-Grained Molecular Dynamics Study

Neila Cristina Fonseca Machado<sup>\*a</sup>, Roberta Albino dos Reis<sup>a</sup>, Renan Silva Nunes<sup>a</sup>, Nicolas A. Garcia<sup>b</sup>, Amedea Barozzi Seabra<sup>a</sup>, and Herculano da Silva Martinho<sup>\*a</sup>

Received Date

Accepted Date

DOI: 00.0000/xxxxxxxxxx

## Abstract

Nitric oxide (NO) delivery across the stratum corneum (SC) remains a major challenge due to the highly ordered, architecture of this skin barrier and the short lifetime of NO. In this work, coarse-grained molecular dynamics simulations are employed to investigate how chitosan-based nanogels loaded with *S*-nitrosoglutathione (GSNO) mediate NO delivery at the SC interface. We used two approaches, with and without the use of a physical enhancer, in this case, a constant electric field. In the absence of an electric field, the chitosan–TPP–GSNO nanogel preserves a cohesive polymeric architecture and adsorbs stably at the membrane surface through protonated chitosan–headgroup interactions. This adsorption induces only mild leaflet compaction, while lamellar thickness and lipid mobility remain essentially unaltered, demonstrating that the nanogel acts as a compliant, surface-anchored reservoir that preserves barrier integrity. Within this architecture, GSNO remains confined in a partially hydrated peripheral region of the nanogel, providing localized interfacial availability of NO without uncontrolled diffusion into the membrane core. Using electric fields, simulations further reveal that external electric fields can actively modulate GSNO behavior by triggering non-equilibrium membrane remodeling events, including vesicle formation and conductive pore opening, which create transient pathways for GSNO transport across the SC. By resolving nanogel structure, interfacial contacts, membrane response, and GSNO trajectories at the molecular level, this study provides an integrated mechanistic picture of how nanogel-mediated confinement and membrane remodeling jointly regulate NO delivery across the stratum corneum.

## 1 Introduction

The stratum corneum (SC) is the outermost layer of human skin and constitutes one of the most effective biological barriers found in nature. Its barrier function originates from a densely packed, multilamellar lipid matrix composed mainly of ceramides, free fatty acids, and cholesterol, organized around corneocytes in a highly ordered architecture<sup>1–4</sup>. While this organization is essential for preventing water loss and external aggression, it also severely restricts the transport of bioactive molecules, making con-

trolled delivery across the SC a long-standing challenge<sup>5–7</sup>.

Nitric oxide (NO) is a short-lived signaling molecule that plays a central role in skin physiology, including regulation of vasodilation, inflammation, wound healing, antimicrobial defense, and tissue regeneration. Localized NO delivery at the skin surface or within superficial layers has therefore attracted significant interest in dermatological, cosmetic, and biomedical applications. However, the high reactivity and short lifetime of NO require delivery strategies based on stable donor molecules, such as *S*-nitrosoglutathione (GSNO), capable of releasing NO in a controlled and spatially confined manner<sup>8?</sup>.

Polymeric nanocarriers have emerged as promising plat-

<sup>a</sup> Centro de Ciências Naturais e Humanas, Universidade Federal do ABC, Av. dos Estados 5001, Santo André-SP, 09210-580, Brazil; E-mail: neila.machado@ufabc.edu.br

forms to modulate skin interfaces without directly compromising barrier integrity. Among them, chitosan-based nanoparticles and nanogels stand out due to their biocompatibility, cationic character, and strong affinity for lipid headgroups. When loaded with GSNO, these systems can act as interfacial reservoirs that position NO donors close to the SC while minimizing uncontrolled diffusion. Experimental studies have demonstrated the effectiveness of chitosan-based NO-releasing nanoparticles in skin-related applications; however, the molecular mechanisms governing how multicomponent chitosan–TPP–GSNO nanogels reorganize at ceramide-rich lipid interfaces remain poorly understood<sup>8,9</sup>.

Molecular dynamics simulations offer a unique and complementary approach to address these questions by explicitly resolving molecular structure, interactions, and dynamics over time. In this context, coarse-grained (CG) molecular dynamics within the Martini force field enables the investigation of large and heterogeneous systems—such as realistic skin-mimetic membranes and polymeric nanocarriers—over extended timescales, while preserving the essential physicochemical interactions governing self-assembly and membrane organization<sup>10–12</sup>. Within this framework, CG simulations have proven particularly powerful in elucidating nanocarrier adsorption, membrane response, and interfacial transport mechanisms in complex lipid barriers<sup>13–15</sup>.

Beyond passive adsorption, external physical stimuli can further modulate transport across highly ordered lipid membranes. Continuous electric fields, in particular, couple directly to membrane polarization and interfacial charge distributions, providing a molecular-level analogue of iontophoresis—a widely used technique that employs low-intensity electric fields to enhance transdermal delivery without catastrophic barrier disruption. At the nanoscale, such fields drive the membrane out of equilibrium and can promote remodeling phenomena such as vesicle budding and pore formation, depending on local stress accumulation and lipid organization<sup>16–18</sup>. In skin-mimetic systems, coarse-grained simulations have shown that continuous electric fields can substantially enhance molecular delivery by inducing vesiculation and conductive pores in SC-like lamellae, thereby opening transient transport pathways that are fundamentally distinct from passive permeation mechanisms<sup>19,20</sup>.

Despite these advances, key molecular questions remain unresolved. It is still unclear (i) how the internal architecture of chitosan–TPP–GSNO nanogels responds to the strong interfacial constraints imposed by the ceramide-rich SC, (ii) which molecular motifs dominate nanogel adhesion at lipid headgroups, (iii) how nanogel adsorp-

tion influences the structural and dynamical properties of the SC membrane, and (iv) how the spatial organization of GSNO within the nanogel governs its potential for interfacial NO delivery. Moreover, the interplay between nanocarrier-mediated interfacial confinement and electric-field–induced membrane remodeling has not been explored within a unified molecular framework.

To address these gaps, the present work employs coarse-grained molecular dynamics simulations to investigate GSNO-derived NO delivery across a realistic stratum corneum model, combining chitosan-based nanogel adsorption with electric-field–driven membrane remodeling. By explicitly resolving nanogel structure, interfacial contact hierarchies, membrane response, and transport pathways at the molecular level, this study establishes mechanistic design principles for controlled NO delivery across highly ordered skin-like lipid barriers.

## 2 Methodology

All molecular dynamics simulations were performed using the GROMACS simulation package<sup>21,22</sup> (versions 2016–2023) within the Martini coarse-grained force field<sup>23,24</sup>. The stratum corneum (SC) membrane model represents the lipid matrix region of human skin and was constructed using the INSANE program<sup>25</sup>. The membrane composition was based on ceramide type II (25%), cholesterol (36%), and tetracosanoic acid (39%), following previously validated SC models<sup>15,26</sup>. Identical lipid compositions were used for the upper and lower leaflets.

Two classes of systems were investigated: (i) SC membranes interacting with free GSNO molecules and (ii) SC membranes interacting with a chitosan–TPP–GSNO nanogel. For the SC + free GSNO systems, the initial simulation box was defined as approximately  $19 \times 19 \times 30 \text{ nm}^3$ . For nanogel-containing systems, a larger simulation box of approximately  $47 \times 47 \times 48 \text{ nm}^3$  was employed to accommodate the full nanogel assembly and its interfacial dynamics.

All systems were solvated using polarizable Martini<sup>27</sup> water beads to provide explicit electrostatic screening, with a relative dielectric constant of  $\epsilon_r = 2.5$ . The polarizable water model ensures appropriate dielectric response in aqueous environments without the need for long-range electrostatics. Sodium and chloride ions were added to reproduce physiological saline conditions ( $[\text{NaCl}] = 0.15 \text{ M}$ ) and to ensure overall electroneutrality.

The chitosan-based nanogel consisted of chitosan chains cross-linked by tripolyphosphate (TPP) and loaded with *S*-nitrosoglutathione (GSNO), which acts as a nitric oxide reservoir. The nanogel was constructed following the same parametrization strategy adopted in our previous work, in

which GSNO remains confined within the nanogel matrix and no free nitric oxide is present at the beginning of the simulations.

All systems were first relaxed in the absence of an external electric field by propagating trajectories for 1000 ns to ensure equilibration of membrane structure organization. After relaxation, the SC + free GSNO system stabilized at a box size of approximately  $18 \times 18 \times 27 \text{ nm}^3$ , was used as starting points for all subsequent simulations with electric field, while the nanogel-containing system reached an equilibrated box size of approximately  $35 \times 35 \times 78 \text{ nm}^3$ .

The equations of motion were integrated using the leap-frog algorithm<sup>28</sup> with an integration time step of 20 fs. Neighbor searching was performed using the Verlet scheme<sup>29</sup>. Electrostatic interactions were treated using the reaction-field method combined with a potential-shift scheme, employing a cutoff radius of 1.1 nm. Van der Waals interactions were modeled using a cutoff-off scheme with potential shifting, also with a cutoff radius of 1.1 nm, consistent with standard Martini parametrization.

Temperature control was achieved using the velocity-rescale (V-rescale) thermostat<sup>30,31</sup>. A target temperature of 306 K was chosen to approximate the temperature of the external human skin. Pressure coupling was performed using the Parrinello–Rahman barostat<sup>32</sup>, with semi-isotropic pressure coupling at 1 atm. The compressibility along the membrane plane was set to  $3 \times 10^{-4} \text{ bar}^{-1}$ . Periodic boundary conditions were applied in all three spatial directions.

Electric-field simulations were carried out by applying constant external electric fields perpendicular to the membrane plane, along the  $z$  direction. The electric-field implementation followed the GROMACS framework as described by Caleman and van der Spoel<sup>33</sup>. Field intensities ranging from 22 to 25 mV nm<sup>-1</sup> were explored. The temporal evolution of each trajectory under an applied field was carefully monitored to identify membrane remodeling events, including pore formation and vesicle budding, which occurred stochastically depending on field strength and local membrane fluctuations.

Structural and dynamical analyses were performed using standard tools available within the GROMACS analysis suite, complemented by custom post-processing scripts when necessary. Nanogel structural stability was assessed through global descriptors such as the radius of gyration and internal contact persistence. Nanogel-membrane interactions were quantified using center-of-mass separations, minimum distances, and bead-level contact statistics. Membrane structural response was characterized by area per lipid, lamellar thickness extracted from density profiles, and lipid tail orientational order parameters. GSNO transport behavior was analyzed at the single-molecule level us-

ing center-of-mass trajectories, depth distributions, mean-squared displacement, and interaction energies with membrane headgroups and tails. All trajectories were periodically visualized using VMD to support and validate the mechanistic interpretations derived from quantitative analyses.

### 3 Results and Discussion

To ensure a coherent interpretation across the wide range of observables generated in this study, we organize the Results and Discussion into two tightly connected parts.

**Part 1** establishes the baseline regime: a chitosan–TPP–GSNO nanogel (NG) interacting with the stratum corneum (SC) membrane *without* an external electric field, which defines barrier-preserving interfacial delivery. **Part 2** evaluates *free* GSNO under constant electric fields and quantifies how membrane remodeling (vesiculation versus pore formation) creates non-equilibrium transport pathways that control delivery efficiency. Across both parts, the analysis progresses from global structural descriptors to single-molecule transport metrics and energetic stabilization, enabling a mechanistic linkage between membrane morphology, molecular confinement, and GSNO/NO delivery.

#### 3.1 Part 1: Barrier-preserving adsorption of the chitosan–TPP–GSNO nanogel on the SC membrane Global structural evolution of the chitosan–TPP–GSNO nanogel

To establish whether the chitosan–TPP–GSNO nanogel can function as a stable carrier at the stratum corneum interface, we first characterized its global structural evolution during the adsorption process. Global descriptors such as the radius of gyration and solvent-accessible surface area provide complementary measures of nanogel compactness, flexibility, and solvent exposure, allowing us to distinguish between transient deformation, interfacial adaptation, and structural destabilization.

The chitosan–TPP–GSNO nanogel (NG) remains structurally robust throughout the 710 ns trajectory, undergoing progressive reorganization as it approaches the SC membrane. The radius of gyration ( $R_g$ ) and solvent-accessible surface area (SASA) (Fig. 1a,b) reveal three distinct regimes. At early times (0–100 ns), the NG displays a compact architecture ( $R_g \sim 7\text{--}10 \text{ nm}$ ; SASA  $\sim 4.8\text{--}5.2 \times 10^3 \text{ nm}^2$ ), consistent with a densely cross-linked chitosan–TPP–GSNO core. Between 100 and 300 ns, both observables increase ( $R_g \approx 12\text{--}14 \text{ nm}$ ; SASA  $\sim 5.5 \times 10^3 \text{ nm}^2$ ), reflecting partial loosening of the polymeric network and increased solvent accessibility of GSNO. Beyond  $\sim 300$  ns, SASA reaches a plateau while  $R_g$  exhibits breathing-like

oscillations (15–20 nm), indicating a flexible yet cohesive interfacial assembly. No signatures of fragmentation or over-swelling are observed, demonstrating that the NG preserves its structural integrity even under interfacial mechanical stress.

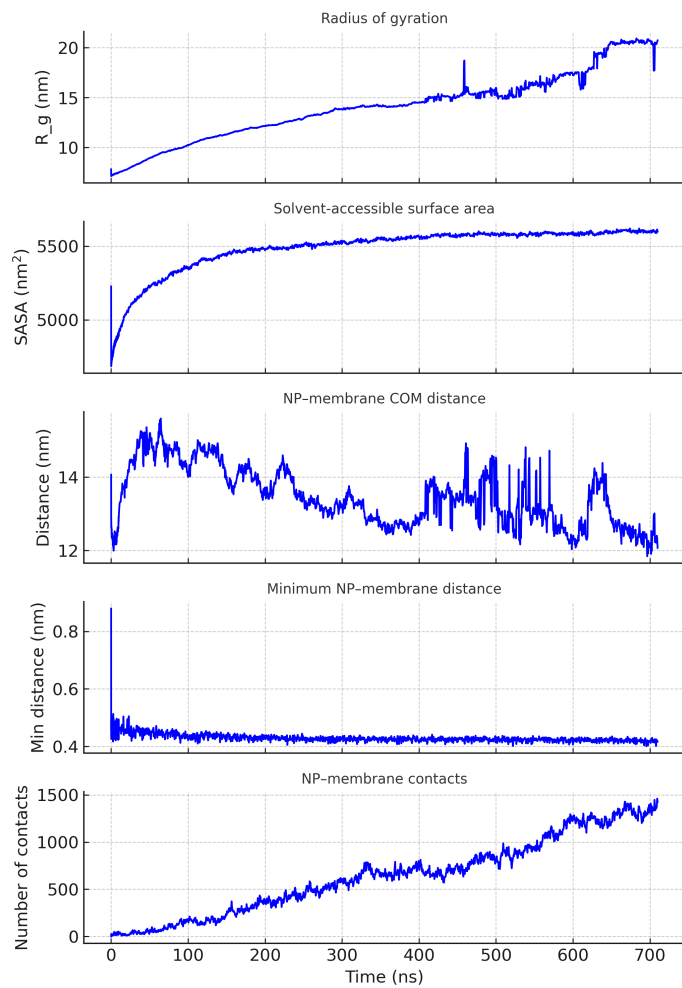


**Fig. 1** Global structural evolution and adsorption dynamics of the chitosan-TPP-GSNO nanogel (NG) at the stratum corneum (SC) membrane interface. (a) Radius of gyration ( $R_g$ ). (b) Solvent-accessible surface area (SASA). (c) NG-membrane center-of-mass (COM) distance. (d) Minimum NG-membrane separation (MINDIST). (e) Total NG-HEADS contacts. Together, these observables show that the NG remains cohesive and structurally adaptable while establishing strong, surface-localized interactions with the SC interface.

### Approach, first contact, and interfacial anchoring

Following the assessment of nanogel structural integrity, we next examined how the nanogel approaches and establishes contact with the SC membrane. To resolve the adsorption pathway at the molecular level, we combined distance-based metrics and contact analyses, which allow us to distinguish long-range electrostatic attraction, initial

surface recognition, and the formation of a persistent interfacial anchoring state.

The adsorption pathway was quantified using three complementary descriptors that probe distinct physical aspects of nanogel-membrane association: the NG-membrane center-of-mass (COM) distance, which reports on long-range approach; the minimum NG-membrane separation (MINDIST), which captures the onset of local molecular contact; and interfacial contact counts, which quantify the progressive consolidation of adhesion (Fig. 1c–e). At early times, the nanogel remains fully solvated in bulk water, with a COM distance exceeding 10 nm, and undergoes smooth diffusive motion toward the membrane surface (Fig. 1c). As the nanogel enters the interfacial region, the MINDIST drops sharply to approximately 0.4–0.45 nm (Fig. 1d), signaling the formation of the first stable bead-level contacts between nanogel components and lipid headgroups. This local contact event coincides with the initial deviations observed in the global structural descriptors ( $R_g$  and SASA), indicating that interfacial recognition triggers nanogel rearrangement. Following this initial anchoring, the number of nanogel-HEADS contacts increases steadily over time (Fig. 1e), reflecting lateral spreading of the nanogel along the membrane surface and the transition from transient contact to a persistent, surface-anchored adsorption state.

Following the initial contact event, nanogel adhesion evolves through a progressive and highly selective interfacial engagement. The total number of NG-HEADS contacts increases monotonically over time, reaching more than 1400 contacts during the final stages of the trajectory, whereas contacts with hydrophobic tail beads remain negligible throughout. This pronounced selectivity demonstrates that nanogel adsorption proceeds via controlled lateral spreading along the polar headgroup region, without penetration into or disruption of the hydrophobic core. Component-resolved analyses further reveal that protonated chitosan chains dominate interfacial adhesion, while GSNO exhibits only intermittent surface sampling and TPP remains largely confined within the nanogel interior.

Leaflet-resolved contact fractions confirm that adsorption remains strictly confined to the outer leaflet of the stratum corneum membrane, excluding any transbilayer engagement or insertion events (see Fig. S4 for detailed contact decompositions).

Together, these observations support a robust three-stage adsorption mechanism comprising (i) long-range electrostatic recognition, (ii) cooperative lateral spreading driven by chitosan-headgroup interactions, and (iii) formation of a persistent, surface-localized anchoring state. This behavior is fully consistent with polymer-mediated interfacial ad-

hesion mechanisms reported for cationic assemblies interacting with ordered lipid matrices<sup>34,35</sup>.

### Vertical positioning and membrane structural response

Once stable interfacial adsorption is established, it is essential to determine the vertical positioning of the nanogel relative to the stratum corneum membrane and to assess whether adsorption perturbs lamellar organization. To address this, we analyzed normalized number density profiles along the membrane normal for nanogel components and membrane lipids (Fig. 2). Chitosan and TPP density maxima are located above the headgroup region, peaking at approximately 25–30 nm, while GSNO displays a broader distribution extending toward the outer headgroup layer. Importantly, no significant overlap with the hydrophobic core is observed, confirming that nanogel adsorption remains strictly interfacial.

Despite sustained surface anchoring, the internal organization of the SC membrane is largely preserved. The area per lipid exhibits only a modest reduction upon nanogel adsorption (from  $0.5544 \pm 0.0156$  to  $0.5425 \text{ nm}^2$ ), consistent with gentle compression of the outer leaflet. Lipid tail ordering remains within the range characteristic of liquid-ordered SC lamellae ( $P_2 = 0.3349 \pm 0.1139$ ), and the headgroup-to-headgroup distance remains constant at approximately 4.49 nm, indicating preserved lamellar thickness.

Lipid lateral mobility is also maintained, as confirmed by subdiffusive mean-squared displacement profiles for ceramides, fatty acids, and cholesterol (Fig. S2). Together, these observations demonstrate that nanogel adsorption induces only elastic, reversible adjustments of the outer leaflet, while preserving the structural and dynamical integrity of the ceramide-rich barrier.

Additional system-level observables, including box relaxation, membrane centering, and leaflet symmetry, confirm elastic equilibration without large-scale deformation (Fig. S1).

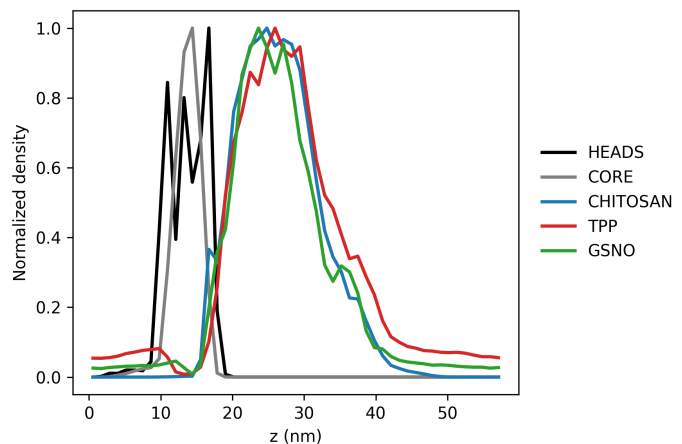


**Fig. 2 Vertical positioning of the chitosan–TPP–GSNO nanogel relative to the stratum corneum membrane.** Normalized number density profiles along the membrane normal for nanogel components (chitosan, TPP, and GSNO) and membrane lipids. Chitosan and TPP remain localized above the headgroup region, while GSNO exhibits a broader distribution extending toward the outer headgroup layer. No overlap with the hydrophobic core is observed, confirming that nanogel adsorption remains strictly interfacial and does not disrupt lamellar organization.

### Internal interaction hierarchy and nanogel architecture

To connect the macroscopic stability and interfacial adaptability of the nanogel to its molecular-level organization, we next examined the internal interaction hierarchy using radial distribution functions (RDFs). RDFs provide a quantitative measure of preferred intermolecular separations and coordination environments, allowing us to identify the dominant cohesive interactions that stabilize the chitosan–TPP–GSNO assembly and to assess the accessibility and hydration state of GSNO within the nanogel matrix.

The RDF analysis reveals a clear hierarchy of interactions governing nanogel architecture (Fig. 3). The most intense and sharply defined peak corresponds to the CHITO( $\text{NH}_3^+$ )–TPP $^{3-}$  pair, located at short intermolecular distances, reflecting strong multivalent electrostatic cross-linking between protonated chitosan chains and tripolyphosphate ions. This interaction constitutes the primary cohesive force responsible for nanogel compaction and long-term structural integrity. In comparison, CHITOSAN–CHITOSAN correlations exhibit broader peaks, consistent with dense but flexible polymer packing, while TPP–TPP RDFs display features indicative of localized TPP-rich microdomains stabilized within the chitosan network.

Interactions involving GSNO are markedly weaker but highly informative. The CHITO( $\text{NH}_3^+$ )–GSNO and CHITOSAN–GSNO RDFs show moderate, short-range association without pronounced long-range ordering, indicat-

ing that GSNO is retained through transient electrostatic and hydrogen-bond-mediated interactions rather than permanent binding. This behavior is consistent with GSNO occupying partially coordinated, solvent-accessible regions near the nanogel periphery, as previously reported for similar chitosan-based assemblies<sup>15</sup>. Importantly, the GSNO–water RDF rapidly approaches unity at short distances, confirming substantial hydration and highlighting that GSNO remains chemically accessible despite being structurally retained within the nanogel.

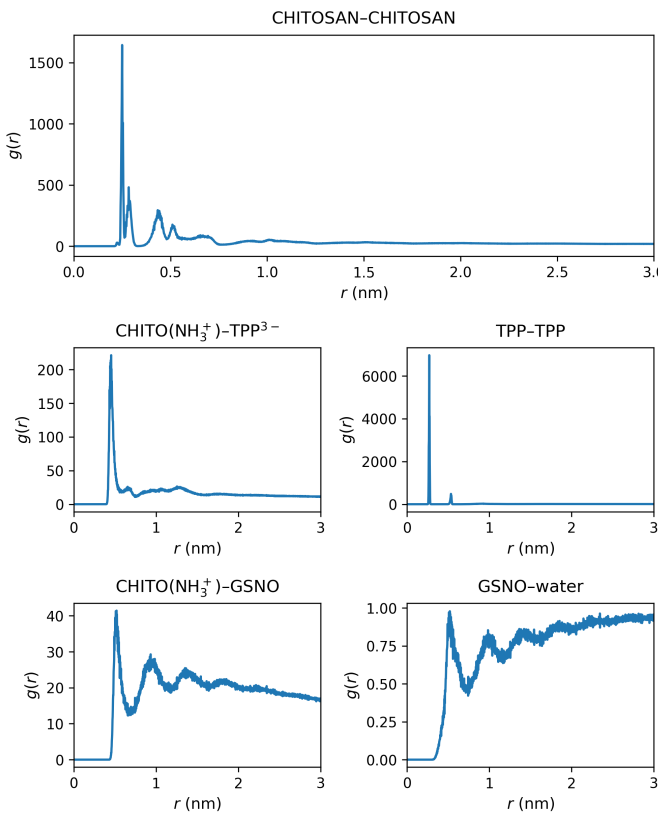


**Fig. 3 Radial distribution functions (RDFs) revealing the internal interaction hierarchy of the chitosan–TPP–GSNO nanogel.** (a) CHITOSAN–CHITOSAN RDF highlighting dense polymer packing within the nanogel matrix. (b) CHITO(NH<sub>3</sub><sup>+</sup>)–TPP<sup>3-</sup> RDF showing a pronounced short-range peak associated with strong multivalent electrostatic cross-linking, which constitutes the primary cohesive interaction stabilizing the nanogel core. (c) TPP–TPP correlations indicating the formation of localized TPP-rich microdomains within the polymer network. (d) CHITO(NH<sub>3</sub><sup>+</sup>)–GSNO RDF revealing moderate association, consistent with partial coordination of GSNO at the periphery of the cross-linked matrix. (e) GSNO–water (PW) RDF approaching bulk-like behavior at short distances, confirming substantial hydration and solvent accessibility of GSNO. Together, these RDFs support a stratified nanogel architecture comprising a strongly cross-linked chitosan–TPP core, a GSNO-enriched interfacial region, and a hydrated outer shell.

Together, these RDFs delineate a stratified nanogel ar-

chitecture comprising (i) a densely cross-linked chitosan–TPP core that provides mechanical cohesion, (ii) a GSNO-enriched intermediate region characterized by moderate retention and high solvent exposure, and (iii) a hydrated outer periphery that facilitates interfacial availability and controlled NO release without nanogel disintegration.

#### Integrated mechanistic model for adsorption and interfacial NO delivery

All descriptors—global NG structure, interfacial distances, contact evolution, density profiles, membrane mechanics, and interaction hierarchy—converge to a unified mechanistic picture. The nanogel approaches the stratum corneum under electrostatic guidance, nucleates adhesion through protonated chitosan domains, spreads laterally while retaining its cross-linked core, and remains confined to the headgroup region without perturbing lamellar thickness or lipid mobility. GSNO resides in a moderately bound, partially hydrated peripheral layer that intermittently samples the interface, providing a physically consistent route for localized NO release at the SC surface<sup>36</sup>. The chitosan–TPP–GSNO nanogel therefore operates as a **non-disruptive, surface-anchored delivery platform**, capable of strong adhesion while preserving barrier integrity—an essential design feature for dermocosmetic and pharmaceutical applications.

While Part 1 establishes the nanogel as a stable interfacial reservoir that localizes GSNO at the membrane surface, effective nitric oxide delivery ultimately depends on the subsequent fate of GSNO after its release from the nanogel matrix. Once GSNO becomes available in the aqueous environment adjacent to the stratum corneum, its transport is no longer governed by nanogel architecture but by direct interactions with the highly ordered, ceramide-rich lipid barrier. Part 2 is therefore designed to isolate and interrogate this next stage of the delivery process by examining the behavior of free GSNO in contact with the SC membrane. By decoupling GSNO transport from nanogel-mediated staging, we resolve how external physical stimuli—specifically continuous electric fields—modulate membrane structure and generate transient pathways that enable GSNO migration across an otherwise impermeable barrier. In this way, Parts 1 and 2 together describe a sequential delivery mechanism, progressing from nanogel-mediated interfacial localization to stimulus-controlled GSNO transport at the membrane level.

In addition to the nanogel-associated population, a fraction of GSNO and TPP molecules is observed to detach from the chitosan network and remain dispersed in the aqueous phase over the course of the simulation. This

behavior is readily apparent from trajectory inspection (Fig. 4) and reflects the dynamic, non-covalent nature of the chitosan–TPP–GSNO assembly rather than nanogel instability. Importantly, the presence of free GSNO does not compromise the structural integrity of the nanogel core, which remains cohesive and surface-anchored throughout the simulation. Instead, this coexistence highlights that the nanogel functions as a regulated reservoir, maintaining a high local concentration of GSNO at the membrane interface while allowing a background population of GSNO to equilibrate with the surrounding solvent. As discussed below, the fate of these free GSNO molecules becomes particularly relevant when external stimuli are applied, motivating their explicit investigation in Part 2.

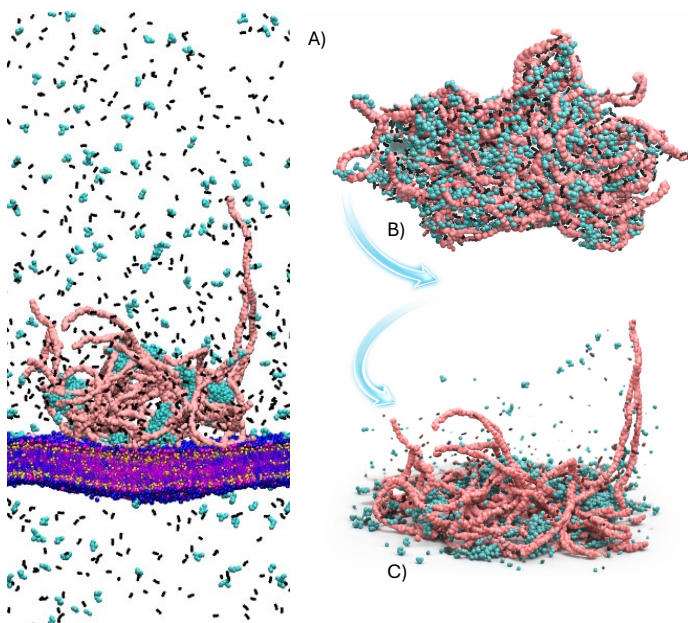


**Fig. 4 Structural states of the chitosan–TPP–GSNO nanogel and its interfacial organization at the stratum corneum.** (A) Final configuration of the nanogel adsorbed at the stratum corneum (SC) surface at the end of the simulation. Chitosan chains are shown in pink, GSNO molecules in cyan, and TPP molecules in black. The nanogel remains surface-anchored while coexisting with a population of GSNO and TPP molecules dispersed in the aqueous phase. (B) Initial configuration of the isolated chitosan–TPP–GSNO nanogel in solution before interaction with the SC membrane, illustrating its compact, self-assembled architecture. (C) Zoomed view of the nanogel extracted from panel (A), highlighting its final internal organization after interfacial adaptation. Together, these panels illustrate the dynamic and non-covalent nature of the nanogel, which preserves a cohesive core upon adsorption while allowing partial release and equilibration of GSNO and TPP in the surrounding solvent, consistent with its role as a regulated interfacial reservoir rather than a closed capsule. Water and ion molecules are omitted for clarity.

### 3.2 Part 2: Free GSNO under electric fields — transport pathways enabled by membrane remodeling

In contrast to the equilibrium, barrier-preserving adsorption regime identified in Part 1, the application of a constant electric field along the membrane normal drives the stratum corneum lamella out of equilibrium and enables GSNO transport through field-induced membrane remodeling. To dissect how this perturbation reconfigures delivery pathways, we combine complementary analyses spanning multiple scales: (i) single-molecule tracking metrics (center-of-mass position, minimum distance, and interfacial contacts), (ii) depth-resolved descriptors (time–depth heatmaps and probability distributions  $P(z)$ ), (iii) mobility signatures from mean-squared displacement, (iv) GSNO–membrane interaction energies, and (v) membrane structural responses, including thickness, tail order, area per lipid, and lateral density maps. For electric-field trajectories, membrane structural analyses are restricted to the 0–100 ns window encompassing the *pre-collapse* and *collapse* regimes (vesicle budding or pore opening), as sustained fields ultimately induce large-scale membrane disintegration for which planar lamellar metrics lose physical meaning.

#### 3.2.1 Baseline behavior: free GSNO without electric field

To establish a reference state for GSNO behavior at the stratum corneum interface, we first analyzed the dynamics of free GSNO in the absence of an external electric field. This baseline enables isolation of intrinsic GSNO–membrane interactions under equilibrium conditions and provides a necessary benchmark against which field-induced transport mechanisms can be unambiguously identified.

The representative trajectory shown in Fig. 5 illustrates the characteristic behavior observed for all GSNO molecules in the control system. As shown in Fig. 5A, the center-of-mass position of  $\text{GSNO}_{25}$  along the membrane normal exhibits broad, continuous fluctuations confined to the aqueous phase, with no sustained drift toward or across the membrane. These excursions reflect unrestricted diffusion in bulk water rather than directed interfacial engagement.

Consistently, interfacial interaction metrics (Fig. 5B) reveal only brief and sporadic approaches to the headgroup region. Transient reductions in the minimum distance to lipid headgroups are accompanied by short-lived contact bursts involving only a few headgroup beads, which rapidly decay as the molecule returns to the bulk solvent. At no point does GSNO display prolonged contact accumulation or stable confinement near the membrane surface.

Together, these descriptors establish that, under equilib-

rium conditions, free GSNO behaves as a fully solvated and highly mobile species with no intrinsic tendency to adsorb, insert into, or traverse the dense ceramide-rich lamella. This baseline behavior demonstrates that spontaneous GSNO penetration is energetically unfavorable and confirms that any sustained interfacial trapping, encapsulation, or translocation observed in subsequent sections arises exclusively from electric-field–induced membrane remodeling rather than from inherent GSNO affinity for the SC membrane.

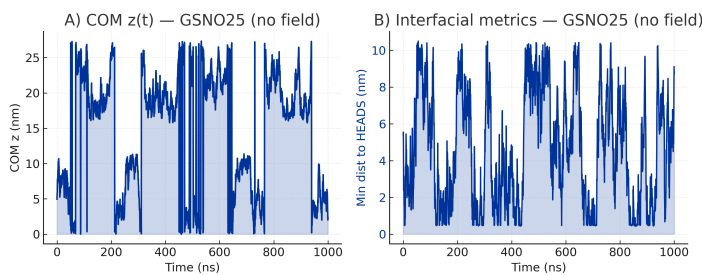


**Fig. 5 Baseline behavior of free GSNO in the absence of an external electric field.** (A) Time evolution of the center-of-mass position along the membrane normal,  $z_{\text{COM}}(t)$ , for GSNO<sub>25</sub>. (B) Interfacial metrics for the same molecule: minimum distance to SC headgroups and number of headgroup contacts. Together, these curves represent the characteristic behavior of GSNO in the control system (no field): a bulk-solvated species that only transiently approaches the headgroup layer, without stable trapping or translocation events.

### 3.2.2 Field-driven bifurcation: vesicle-mediated capture versus pore-mediated conduction

Having established the equilibrium behavior of free GSNO at the stratum corneum interface, we next investigated how a constant external electric field perturbs the membrane and reshapes the available transport pathways. Because electric-field-induced membrane remodeling is intrinsically stochastic, a large ensemble of independent trajectories is required to distinguish robust mechanistic trends from isolated events. We therefore analyzed a statistically meaningful set of simulations to identify recurrent membrane response modes and to assess their relative occurrence across the explored range of field intensities.

In total, 65 simulations were performed, spanning 13 electric-field intensities ( $0.0220\text{--}0.0250 \text{ V nm}^{-1}$ ) with five independent random seeds per condition. Across this ensemble, two distinct classes of membrane response were consistently observed: (i) vesicle budding, in which a membrane-derived compartment encapsulates one or more GSNO molecules, and (ii) conductive pore formation, in which a continuous, headgroup-lined aqueous channel spans the membrane. Pore formation represents the dom-

inant outcome, occurring in 58 of 65 trajectories (89%), whereas vesiculation is less frequent, appearing in 7 trajectories (11%). Among vesicular events, capture of a single GSNO molecule (V(1)) is most common, while encapsulation of two molecules (V(2)) is comparatively rare.

Importantly, both vesicle formation and pore formation are observed within the same range of electric-field intensities, indicating that these outcomes do not correspond to strictly separated regimes but rather to competing, stochastic membrane responses to the applied field. Vesiculation is preferentially detected in the low-to-intermediate field range ( $0.0220\text{--}0.0228 \text{ V nm}^{-1}$ ), where the field induces sufficient interfacial stress to promote local curvature and budding without stabilizing a continuous aqueous conduit. At higher field strengths, pore formation becomes increasingly prevalent, consistent with enhanced polarization and stabilization of hydrophilic nanochannels across the ceramide-rich lamella.

These observations demonstrate that the electric field does not simply enhance GSNO affinity for the membrane but instead acts as a pathway selector, biasing the membrane toward distinct non-lamellar morphologies that enable transport. Vesicle-mediated capture provides a selective but low-throughput mechanism, whereas pore-mediated conduction offers a continuous, higher-throughput pathway for GSNO migration. A complete trajectory-by-trajectory breakdown of membrane responses and random seeds is provided in Table S1.

### 3.2.3 Vesicle-mediated GSNO capture and transport

Among the membrane remodeling responses induced by the electric field, vesicle formation represents a selective transport pathway in which GSNO can become transiently or permanently encapsulated within a membrane-derived compartment. To resolve this mechanism beyond population-averaged descriptors, we analyzed GSNO transport at the single-molecule level by correlating axial motion with interfacial distance and contact metrics during vesicle nucleation and detachment.

Individual tracking of all 20 GSNO molecules reveals that most remain fully solvated in the aqueous phase, while a small subset displays pronounced but transient interfacial interactions with the membrane. These molecules frequently approach the headgroup region and form short-lived contact bursts, yet do not undergo true encapsulation, instead residing on the outer leaflet or on the external surface of the vesicle. In contrast, a single GSNO molecule (resid 69217) exhibits a trajectory fully consistent with vesicle-mediated capture, as illustrated in Fig. 6.

As shown in Fig. 6A, the center-of-mass position of GSNO<sub>69217</sub> along the membrane normal displays three dis-

tinct regimes: an initial bulk-solvated phase characterized by diffusive motion, a short-lived capture window coinciding with vesicle neck formation, and a subsequent long-lived confinement inside the vesicle lumen that migrates across the simulation box under periodic boundary conditions. This transition is accompanied by a sharp decrease in the minimum distance to lipid headgroups and a concomitant increase in the number of simultaneous headgroup contacts (Fig. 6B), providing a quantitative signature of true vesicular encapsulation rather than transient surface adsorption.

These observations underscore a key methodological point: population-averaged observables alone are insufficient to identify rare but mechanistically relevant transport events. Unambiguous discrimination between interfacial sampling and genuine vesicle-mediated transport requires *per-molecule* analysis combining center-of-mass trajectories, minimum-distance metrics, contact statistics, and direct structural visualization.

### 3.2.4 Pore-mediated GSNO conduction

In contrast to vesicle-mediated transport, pore formation provides a continuous, headgroup-lined pathway that enables GSNO migration directly across the stratum corneum membrane. To characterize this mechanism at the molecular level, we analyzed representative GSNO trajectories displaying sustained axial displacement and correlated their motion with interfacial proximity and contact persistence within the pore environment.

A representative example is shown for GSNO<sub>69221</sub> in Fig. 7. As illustrated in Fig. ??C, the center-of-mass position along the membrane normal exhibits a continuous, monotonic drift over time, in sharp contrast to the bounded diffusive excursions observed in the no-field control (Fig. 5). This behavior reflects genuine axial conduction rather than transient interfacial sampling or vesicular capture.

The interfacial nature of this transport pathway is further resolved by the metrics shown in Fig. ??D. Throughout the conduction event, GSNO maintains persistent subnanometer proximity to lipid headgroups and sustains a high number of simultaneous headgroup contacts. These features indicate that GSNO migrates while remaining tightly coupled to a hydrated, headgroup-rich environment lining the pore interior, rather than diffusing through bulk-like solvent.

Together, the correlated axial drift and sustained interfacial engagement provide direct evidence that pore-mediated transport proceeds via an “interfacial sliding” mechanism along the walls of a hydrophilic nanochannel. Unlike vesicular transport, which relies on selective encapsulation and collective membrane motion, pore-mediated

conduction offers a continuous, higher-throughput pathway in which GSNO exploits the polar architecture of the electroporation pore. This mode of transport is energetically favorable for amphiphilic molecules such as GSNO and is consistent with established molecular descriptions of electric-field-induced membrane pores.

### 3.2.5 Depth heatmaps, $P(z)$ , and mobility: population-level signatures of GSNO transport

While single-molecule trajectories provide detailed mechanistic insight into individual GSNO transport events, population-level descriptors are required to systematically compare transport behavior across distinct membrane remodeling regimes. To this end, we analyzed depth-time heatmaps, depth probability distributions  $P(z)$ , and mean-squared displacement (MSD) profiles, which together capture the collective signatures of bulk diffusion, vesicular confinement, and pore-mediated conduction.

In the absence of an external electric field, GSNO exhibits a broad and diffuse depth-time distribution, consistent with unrestricted bulk diffusion and only transient excursions toward the headgroup region. The corresponding  $P(z)$  profile remains wide and bulk-centered, while the MSD displays slow, diffusion-dominated growth, reflecting the absence of sustained membrane engagement.

Under vesicle-forming conditions, population-level descriptors reveal a qualitatively different transport mode. GSNO depth-time trajectories collapse into a narrow, long-lived band following vesicle capture, indicating strong spatial confinement within a membrane-derived compartment. This confinement is reflected in a sharply peaked  $P(z)$  distribution and a rapidly increasing MSD, consistent with advective transport driven by vesicle migration rather than molecular diffusion.

In contrast, pore-forming conditions produce an intermediate but distinct signature. Depth-time heatmaps display a continuous axial progression along the membrane normal, and  $P(z)$  extends across multiple depths, reflecting sustained sampling of the pore interior. MSD growth is intermediate between bulk diffusion and vesicular transport, consistent with directed axial motion constrained by interfacial sliding along a hydrated, headgroup-lined nanochannel.

Together, these population-level observables delineate three distinct GSNO transport regimes controlled by membrane remodeling: equilibrium bulk diffusion in the absence of field, selective confinement and advective transport via vesicles, and continuous, higher-throughput conduction through electric-field-induced pores. For clarity and completeness, the full set of MSD curves, depth distributions, and depth-time heatmaps supporting this analysis

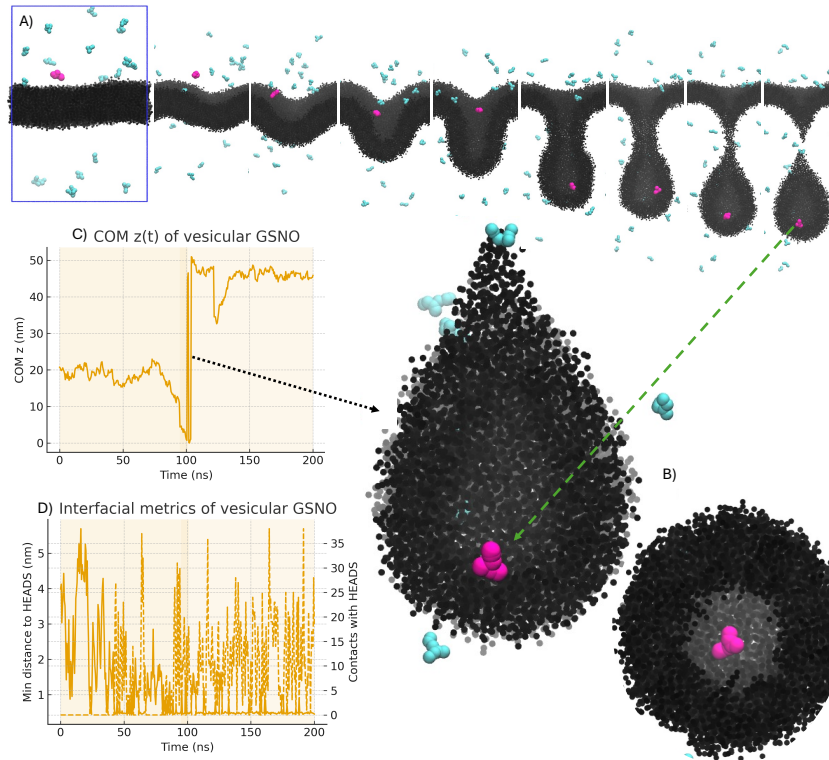


**Fig. 6 Electric-field–induced vesicular capture of a single GSNO molecule (resid 69217).** (A) Time-resolved molecular rendering of vesicle nucleation and detachment from the stratum corneum membrane under an applied electric field. Lipid headgroups and tails progressively curve to form a neck that pinches off into a detached vesicle. GSNO molecules are shown in cyan, and the tracked GSNO<sub>69217</sub> molecule is highlighted in magenta to emphasize its fate during vesicle formation. Water molecules are omitted for clarity. (B) Zoomed views of the detached vesicle containing GSNO<sub>69217</sub>. Two representative snapshots are shown: immediately after vesicle scission from the membrane and at a later time point, demonstrating persistent confinement of the molecule within the vesicle lumen after detachment. Water molecules are omitted for clarity. (C) Center-of-mass trajectory  $z_{\text{COM}}(t)$  of GSNO<sub>69217</sub> along the membrane normal, revealing three distinct regimes: bulk diffusion in the aqueous phase, rapid capture coinciding with vesicle neck formation, and long-lived confinement after vesicle budding. (D) Interfacial interaction metrics for the same molecule, including the minimum distance to lipid headgroups and the number of simultaneous headgroup contacts. The capture window is marked by a sharp reduction in minimum distance and a pronounced increase in contacts, providing a quantitative signature of true vesicular encapsulation rather than transient surface adsorption.

is provided in Fig. S7 of the Supporting Information.

### 3.2.6 Energetic stabilization: GSNO–membrane interaction energies

Because GSNO transport across the SC membrane is governed not only by geometry but also by local energetic stabilization, we next examined short-range GSNO–membrane interaction energies. Lennard–Jones (LJ) contributions were analyzed to quantify how GSNO stabilization differs between bulk, vesicular, and pore-associated environments.

The time evolution of GSNO–HEADS and GSNO–TAILS LJ interactions is shown in Fig. 8. In the absence of an electric field, GSNO exhibits weak and relatively steady stabilization dominated by occasional headgroup contacts, consistent with transient interfacial sampling without sustained membrane engagement. Under vesicle-forming con-

ditions, GSNO experiences the strongest and most fluctuating stabilization, reflecting extensive contact with curved, reorganized lipid environments during vesicle wrapping and confinement. In the pore-forming regime, stabilization is intermediate, consistent with repeated but spatially constrained interactions along the pore walls during interfacial sliding.

These trends are summarized quantitatively in Fig. 9, which reports average LJ stabilization over the 0–200 ns window. Vesicle-mediated transport yields the deepest energetic stabilization, pore-mediated conduction produces moderate stabilization, and the control remains the weakest. This energetic hierarchy mirrors the mobility and depth-distribution signatures, reinforcing the interpretation that membrane remodeling—not intrinsic GSNO affinity—governs transport efficiency.

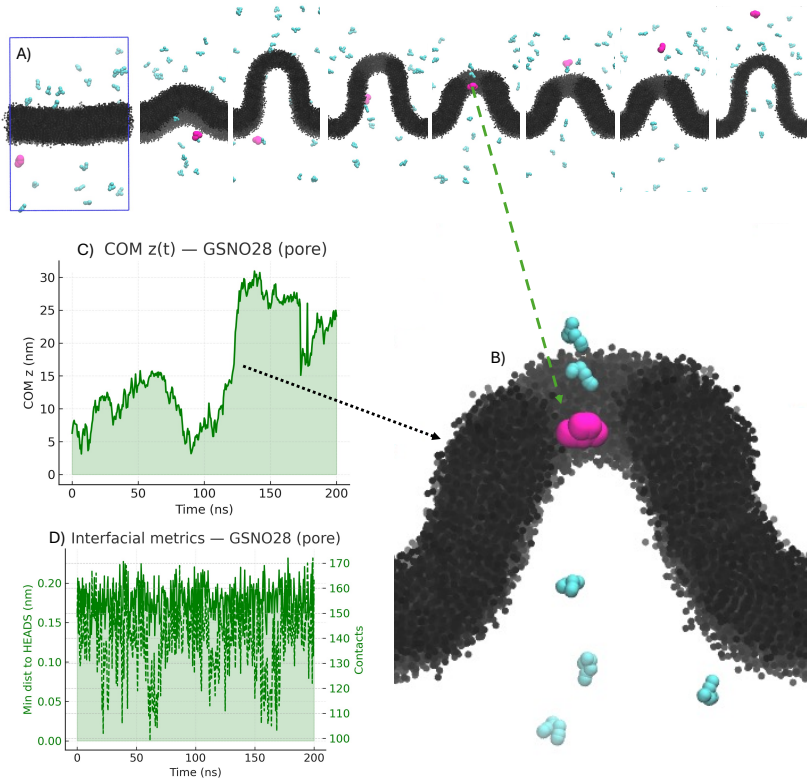


**Fig. 7 Translocation of a GSNO molecule through an electric-field-induced pore in the stratum corneum membrane.** (A) Time-resolved molecular rendering of electric-field-induced pore formation in the stratum corneum membrane and subsequent GSNO translocation. The applied field promotes local membrane thinning and hydration, leading to the nucleation of a headgroup-lined aqueous pore. GSNO molecules are shown in cyan, and the tracked GSNO<sub>69221</sub> molecule is highlighted in magenta to emphasize its trajectory through the evolving pore structure. Water molecules are omitted for clarity. (B) Zoomed view of the hydrated pore during active translocation, highlighting the spatial confinement of GSNO<sub>69221</sub> within the headgroup- and lipid-lined nanochannel and its close association with the pore interior. Water molecules are omitted for clarity. (C) Time evolution of the GSNO center-of-mass position along the membrane normal,  $z_{\text{COM}}(t)$ , for GSNO<sub>69221</sub>, showing a continuous axial drift promoted by the applied electric field during the simulation time. (D) Interfacial metrics for the same molecule: minimum distance to lipid headgroups (solid line) and number of headgroup contacts (dashed line). Persistent sub-nanometer proximity and sustained contact indicate that GSNO migrates in a strongly interfacial manner along the hydrated pore interior. Together, these panels support a mechanistic picture of pore-mediated transport driven by electric-field-induced formation of a hydrophilic nanochannel.

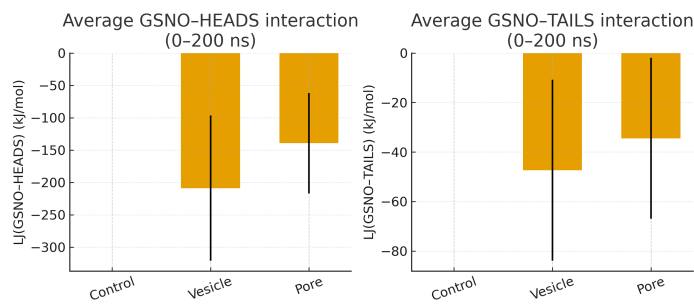


**Fig. 9 Average Lennard-Jones stabilization of GSNO at membrane environments (mean  $\pm \sigma$ ) over 0–200 ns.** Bars show mean LJ(GSNO-HEADS) and LJ(GSNO-TAILS), with error bars denoting standard deviation. Vesicle formation produces the deepest stabilization, pore formation yields intermediate stabilization, and the control is weakest, supporting the transport hierarchy inferred from mobility and depth distributions.

### 3.2.7 Membrane response under electric field: thickness, order, APL, and lateral density maps

To connect GSNO transport behavior with the underlying membrane remodeling, we quantified electric-field-induced changes in SC membrane structure during the early-time window encompassing vesicle budding or pore opening, where planar lamellar descriptors remain physically meaningful.

Analysis of headgroup-to-headgroup distances indicates that the control SC lamella remains compact ( $D_{\text{HH}} \approx 4.49$  nm). Vesicle-forming conditions produce a pronounced apparent thickening ( $D_{\text{HH}} \approx 7.50$  nm), consistent with strong curvature and headgroup redistribution during budding, whereas pore-forming conditions yield a more

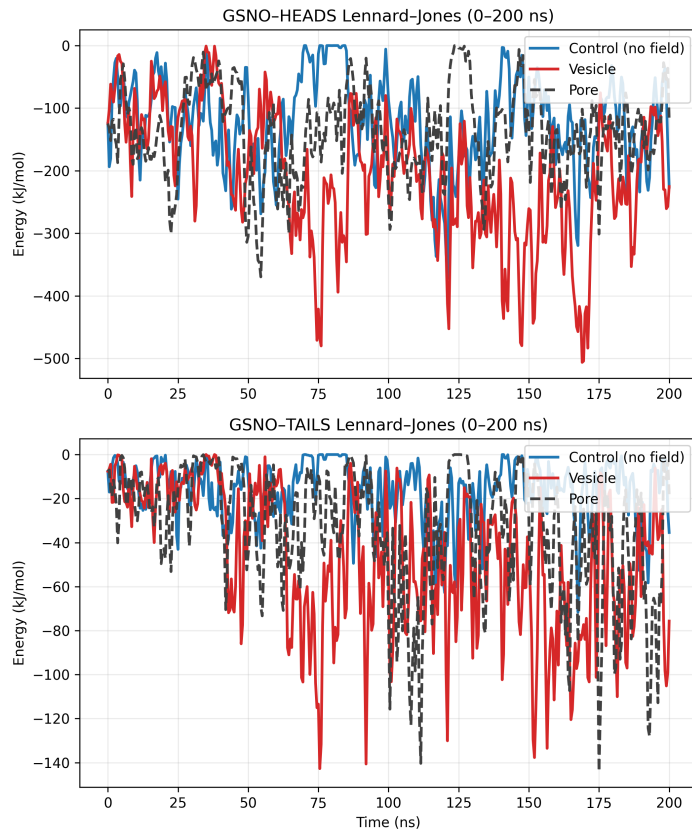


**Fig. 8 Time evolution of short-range Lennard-Jones interaction energies between GSNO and the SC membrane over the initial 200 ns. (A) LJ-SR(GSNO-HEADS). (B) LJ-SR(GSNO-TAILS).** Vesicle-forming conditions show the strongest stabilization and the largest fluctuations, consistent with lipid wrapping and confinement. Pore-forming conditions yield intermediate stabilization associated with sustained pore-wall interactions (interfacial sliding). The control remains comparatively weaker and steadier, consistent with predominantly bulk-like behavior.

moderate increase ( $D_{\text{HH}} \approx 5.86 \text{ nm}$ ), reflecting localized axial dilation around the nascent conductive channel.

Tail orientational order decreases sharply under electric-field perturbation. While the control exhibits high alignment ( $P_2 = 0.4296 \pm 0.0083$ ), both vesicle and pore regimes display strongly reduced order ( $P_2 = 0.1435 \pm 0.1205$  and  $P_2 = 0.1085 \pm 0.1437$ , respectively), indicating substantial loss of lamellar alignment during remodeling.

Consistent with these changes, the area per lipid (APL) remains stable in the control system ( $\text{APL} = 0.3367 \pm 0.0020 \text{ nm}^2$ ) but decreases markedly under electric fields (Fig. 10). Vesicle-forming trajectories show the strongest reduction and fluctuations ( $\text{APL} = 0.2143 \pm 0.0802 \text{ nm}^2$ ), whereas pore-forming trajectories retain higher average APL values ( $\text{APL} = 0.2843 \pm 0.0295 \text{ nm}^2$ ), consistent with more localized disruption.

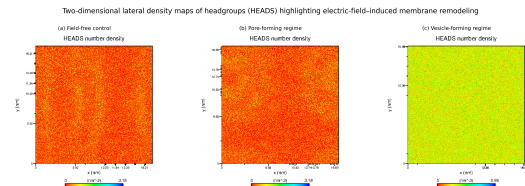


**Fig. 11 Two-dimensional lateral density maps of headgroups (HEADS) highlighting electric-field-induced membrane remodeling.** (a) Field-free control, showing a homogeneous lateral distribution of headgroups characteristic of a stable lamellar barrier. (b) Pore-forming regime, where a localized region of reduced headgroup density corresponds to a conductive aqueous pore and lipid accumulation at its rim. (c) Vesicle-forming regime, displaying pronounced lateral heterogeneity and displaced high-density clusters consistent with vesicle budding and detachment. All density maps are XY projections integrated over Z and computed over 0–100 ns for electric-field systems.

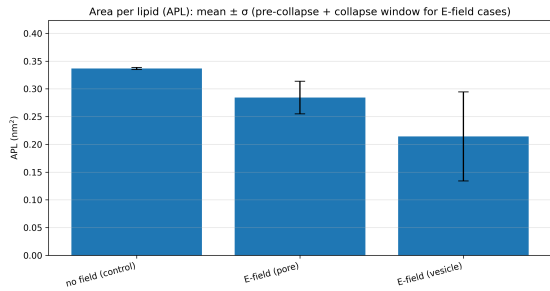


**Fig. 10 Electric-field-induced lateral reorganization quantified by the area per lipid (APL) over 0–100 ns.** Bars show mean APL values, and error bars denote standard deviation. The control remains tightly packed and stable, whereas vesicle and pore regimes exhibit reduced APL and enhanced fluctuations, reflecting field-induced non-lamellar remodeling during the pre-collapse and collapse window (vesicle budding or pore opening).

Direct real-space evidence for these distinct remodeling pathways is provided by the two-dimensional lateral headgroup density maps shown in Fig. 11. The control system displays a homogeneous lateral distribution characteristic of an intact lamella. Pore-forming conditions exhibit a localized depletion surrounded by headgroup accumulation, consistent with pore nucleation. In contrast, vesicle-forming conditions display pronounced lateral heterogeneity and displaced dense clusters, reflecting large-scale lipid redistribution during vesicle budding and detachment.

Together, these structural descriptors establish a coherent physical picture: pore formation corresponds to a localized topological defect that enables conductive GSNO transport while partially preserving lamellar organization, whereas vesiculation represents a more disruptive remodeling pathway associated with selective cargo capture and collective membrane motion.

Taken together, the results presented in Parts 1 and 2 define a unified mechanistic framework in which GSNO/NO delivery across lipid barriers emerges from the interplay between interfacial confinement, barrier architecture, and external physical stimuli. In this context, comparison with our previous tomato cuticle model provides a useful reference for understanding how barrier composition modulates interfacial accessibility, rather than constituting an independent system of analysis.

In moderately ordered cuticular membranes enriched with  $\beta$ -carotene, NO and GSNO exhibit an intrinsically interfacial character, maintaining stable interactions with polar groups while avoiding deep insertion into the hydrophobic core. Such behavior supports localized chemical reactivity at the interface without compromising barrier integrity and reflects the comparatively looser packing of the cuticular lipid matrix. In contrast, the stratum corneum membrane analyzed here is highly cohesive and ceramide-rich, and free GSNO remains effectively excluded from the interface under equilibrium conditions (Fig. 5). In this case, external physical activation is required to unlock delivery pathways by inducing transient non-lamellar membrane remodeling.

Importantly, the applied electric field does not simply enhance GSNO affinity for the membrane. Rather, it acts as a pathway selector that enables two physically distinct transport mechanisms: selective vesicle-mediated capture (Fig. 6) and continuous pore-mediated conduction (Fig. ??), consistent with the outcome statistics summarized in Table ???. These mechanisms differ fundamentally in throughput, selectivity, and membrane perturbation, underscoring that GSNO transport across the SC is governed by remodeling-induced topology rather than passive permeation.

Within this broader framework, the chitosan–TPP–GSNO nanogel investigated in Part 1 plays a crucial staging role. By acting as a stable, barrier-preserving interfacial reservoir, the nanogel positions GSNO in a hydrated and chemically accessible peripheral environment while preventing uncontrolled penetration or membrane disruption (Figs. 1–3). Part 2 then demonstrates how such interfacial availability can be converted into active delivery when external stimuli generate vesicles or pores that capture or conduct GSNO across the membrane. Together, these results highlight a general design principle for NO delivery across lipid barriers: effective transport arises from interfacial confinement coupled to stimulus-controlled activation of transient pathways, with the nanogel providing a robust and non-disruptive platform for controlled delivery.

## 4 Conclusions

### 5 Conclusions

This study establishes a unified molecular framework describing how GSNO/NO delivery across the stratum corneum (SC) lipid barrier can be modulated by coupling nanocarrier-mediated interfacial staging with stimulus-driven transport activation. Using coarse-grained molecular dynamics simulations, we demonstrate that effective delivery does not arise from passive permeation but from a controlled interplay between nanogel architecture, membrane organization, and externally induced membrane remodeling.

In the absence of external fields (Part 1), the chitosan–TPP–GSNO nanogel responds to interfacial constraints by preserving a cohesive polymeric architecture dominated by strong multivalent chitosan–TPP cross-linking, while undergoing controlled lateral adaptation at the membrane surface. Adsorption is mediated primarily by protonated chitosan chains interacting with ceramide-rich headgroups, leading to stable anchoring without penetration into the hydrophobic core. Importantly, nanogel adsorption induces only mild leaflet compaction and modest ordering changes, while preserving lamellar thickness and lipid mobility, demonstrating that the SC barrier remains structurally and dynamically intact.

Within this interfacial regime, GSNO is retained in a partially hydrated, peripheral nanogel environment that intermittently samples the membrane interface. This spatial organization underpins the potential for localized interfacial NO delivery, while preventing uncontrolled diffusion of GSNO or NO into the bulk or across the membrane.

When GSNO is present as a free molecule under an applied electric field (Part 2), delivery is governed not by intrinsic affinity but by field-induced membrane remodeling. Vesicle-mediated capture and pore-mediated conduction emerge as distinct transport pathways, differing in selectivity, throughput, and membrane perturbation. Single-molecule trajectories, depth distributions, mobility metrics, interaction energetics, and membrane structural descriptors consistently show that GSNO transport proceeds via transient non-lamellar structures rather than passive permeation through the ordered SC matrix.

Overall, this work defines clear design principles for controlled NO delivery across highly ordered lipid barriers: nanogel architecture governs barrier-preserving interfacial staging, while external stimuli can be used to selectively activate transport pathways when deeper delivery is required. By explicitly linking nanocarrier structure, membrane response, and transport mechanism, these results provide a rational foundation for the development of next-

generation NO-delivery platforms in dermocosmetic, pharmaceutical, and biomedical applications.

## Conflicts of interest

There are no conflicts to declare.

## Acknowledgements

The authors would like to thank the financial support of the Brazilian agency Conselho Nacional de Desenvolvimento Científico e Tecnológico (CNPq) procs.311933/2021-1, 406761/2022-1 (INCT INTERAS), 401604/2022-5. The authors would also thank the computational resources provided by Sistema de Computação Petaflópica (Tier 0) (Santos Dumont-LNCC) under Sistema Nacional de Processamento de Alto Desempenho (SINAPAD) of the Ministério da Ciência, Tecnologia e Inovação (MCTI), Multi-user Central Facilities of UFABC (CEM-UFABC), and Multi-user Computing Center (CCM/Propes) of UFABC. We thank Angelescu, D. G., for readily providing the chitosan modeling data used in this study.

## Rereferences

- 1 P. M. Elias, *Journal of Investigative Dermatology*, 1983, **80**, 44–49.
- 2 P. W. Wertz, *Acta Dermato-Venereologica*, 2000, **80**, 7–11.
- 3 J. A. Bouwstra and M. Ponec, *Biochimica et Biophysica Acta (BBA) - Biomembranes*, 2003, **1758**, 2080–2095.
- 4 L. Norlén, *Journal of Investigative Dermatology*, 2001, **117**, 830–836.
- 5 R. O. Potts and R. H. Guy, *Pharmaceutical Research*, 1992, **9**, 663–669.
- 6 J. Hadgraft, *International Journal of Pharmaceutics*, 2001, **224**, 1–18.
- 7 S. Mitragotri, P. A. Burke and R. Langer, *Nature Reviews Drug Discovery*, 2011, **10**, 531–546.
- 8 A. B. Seabra and N. Durán, *Journal of Materials Chemistry*, 2010, **20**, 1624–1637.
- 9 R. S. Nunes, V. D. P. Cinel, J. C. Pieretti, K. C. F. Mariano and A. B. Seabra, *Journal of Materials Chemistry B*, 2025.
- 10 S. J. Marrink, H. J. Risselada, S. Yefimov, D. P. Tieleman and A. H. de Vries, *The Journal of Physical Chemistry B*, 2007, **111**, 7812–7824.
- 11 H. I. Ingólfsson, C. A. Lopez, J. J. Uusitalo, D. H. de Jong, S. M. Gopal, X. Periole and S. J. Marrink, *Wiley Interdisciplinary Reviews: Computational Molecular Science*, 2014, **4**, 225–248.
- 12 S. J. Marrink, V. Corradi, P. C. T. Souza, H. I. Ingólfsson, D. P. Tieleman and M. S. P. Sansom, *Chemical Reviews*, 2019, **119**, 6184–6226.
- 13 M. Venturoli, B. Smit and M. M. Sperotto, *Physical Chemistry Chemical Physics*, 2006, **8**, 1139–1150.
- 14 B. M. H. Bruininks, P. C. T. Souza and S. J. Marrink, *Methods in Molecular Biology*, 2018, **2022**, 105–127.
- 15 N. Machado, B. M. H. Bruininks, P. Singh, L. Dos Santos, C. Dal Pizzol, G. C. Dieamant, O. Kruger, A. A. Martin, S.-J. Marrink, P. C. T. Souza and P. P. Favero, *Nanoscale*, 2022, **14**, 506–514.
- 16 J. C. Weaver and Y. A. Chizmadzhev, *Bioelectrochemistry and Bioenergetics*, 1996, **41**, 135–160.
- 17 D. P. Tieleman, *BMC Biochemistry*, 2004, **5**, 10.
- 18 P. T. Vernier, M. J. Ziegler, Y. Sun, M. A. Gundersen and D. P. Tieleman, *Biochimica et Biophysica Acta (BBA) - Biomembranes*, 2013, **1828**, 156–165.
- 19 N. Machado, C. Callegaro, M. A. Christoffolete and H. da Silva Martinho, *Physical Chemistry Chemical Physics*, 2021, **23**, 8273–8281.
- 20 N. Machado, D. Araujo, L. Ruano, V. F. Palmisano, N. Anguita-Ortiz, C. C. S. Bandeira, R. Borges, J. J. Nogueira and H. Martinho, *Physical Chemistry Chemical Physics*, 2025, **27**, 8824–8832.
- 21 M.J. Abraham, D. van der Spoel, E. Lindahl, B. Hess, the GROMACS and D. Team, 2018.
- 22 D. Van Der Spoel, E. Lindahl, B. Hess, G. Groenhof, A. E. Mark and H. J. C. Berendsen, *Journal of Computational Chemistry*, 2005, **26**, 1701–1718.
- 23 S.-J. Marrink, H. J. Risselada, S. Yefimov, D. P. Tieleman and A. H. de Vries, *Journal of Physical Chemistry B*, 2007, **111**, 7812–7824.
- 24 S.-J. Marrink, A. H. de Vries and A. E. Mark, *Journal of Physical Chemistry B*, 2004, **108**, 750–760.
- 25 T. A. Wassenaar, H. I. Ingólfsson, R. A. Böckmann, D. P. Tieleman and S. J. Marrink, *J. Chem. Theory Comput.*, 2015, **11**, 2144–2155.
- 26 N. C. F. Machado, L. dos Santos, B. G. Carvalho, P. Singh, C. A. Téllez Soto, N. G. Azoia, A. Cavaco-Paulo, A. A. Martin and P. P. Favero, *Computers in Biology and Medicine*, 2016, **75**, 151–159.
- 27 S. O. Yesylevskyy, L. V. Schäfer, D. Sengupta and S. J. Marrink, *PLoS computational biology*, 2010, **6**, e1000810.
- 28 R. Hockney, S. Goel and J. Eastwood, *Journal of Computational Physics*, 1974, **14**, 148–158.
- 29 L. Verlet, *Physical Review*, 1967, **159**, 98–103.
- 30 G. Bussi, D. Donadio and M. Parrinello, *The Journal of chemical physics*, 2007, **126**, 014101.
- 31 H. J. C. Berendsen, J. P. M. Postma, W. F. van Gunsteren, A. DiNola and J. R. Haak, *The Journal of Chemical Physics*, 1984, **81**, 3684–3690.

- 32 M. Parrinello and A. Rahman, *Journal of Applied Physics*, 1981, **52**, 7182–7190.
- 33 C. Caleman and D. Van Der Spoel, *Angew. Chem. Int. Ed.*, 2008, **47**, 1417–1420.
- 34 I. Adroher-Benítez, J. Oliveira, A. Córdoba, Y. Feng, J. J. De Pablo, M. Müller and L. da Silva, *Macromolecules*, 2023, **56**, 10285–10295.
- 35 S. Banerjee, L. Schöne, S. Förster and C. Holm, *Journal of Physical Chemistry B*, 2017, **121**, 8638–8651.
- 36 A. B. Seabra, P. S. Haddad and R. S. da Silva, *Brazilian Journal of Medical and Biological Research*, 2004, **37**, 583–594.